Acta Astronautica 119 (2016) 101–109

Contents lists available at ScienceDirect

Acta Astronautica

journal homepage: www.elsevier.com/locate/actaastro

An approximate model for pulsar navigation simulation ☆

Ilija Jovanovic *, John Enright

350 Victoria Street, Toronto, Ontario, Canada

ARTICLE INFO

Article history:
Received 13 February 2015
Received in revised form
6 July 2015
Accepted 4 November 2015
Available online 14 November 2015

Keywords:
Pulsar navigation
Simulation
Approximation

ABSTRACT

This paper presents an approximate model for the simulation of pulsar aided navigation systems. High fidelity simulations of these systems are computationally intensive and impractical for simulating periods of a day or more. Simulation of yearlong missions is done by abstracting navigation errors as periodic Gaussian noise injections. This paper presents an intermediary approximate model to simulate position errors for periods of several weeks, useful for building more accurate Gaussian error models. This is done by abstracting photon detection and binning, replacing it with a simple deterministic process. The approximate model enables faster computation of error injection models, allowing the error model to be inexpensively updated throughout a simulation. Testing of the approximate model revealed an optimistic performance prediction for non-millisecond pulsars with more accurate predictions for pulsars in the millisecond spectrum. This performance gap was attributed to noise which is not present in the approximate model but can be predicted and added to improve accuracy.

1. Introduction

Pulsar navigation (PN) is a method of orbit determination whose precision is not affected by distance from Earth. Other methods commonly used for orbit determination are global positioning system (GPS), two-way Doppler, range finding, and delta-differential one-way ranging (ΔDOR). PN is not able to compete with the accuracy of GPS, however, GPS is only available to spacecraft near Earth [1,2]. Within the inner solar system, PN offers an OD system which can compete with the performance of two-way Doppler, range finding, and (ΔDOR) [3,4]. Since the accuracy of any Earth based tracking system deteriorates with distance, PN could be beneficial to missions venturing past the orbit of Jupiter (6 AU from Earth) [5,6]. Not having to rely on contact with the Earth means PN could potentially offer better latency and availability than other OD methods. Table 1 shows performance estimates of the above systems.

Simulation of missions using PN can be time consuming, on the order of real-time. With suitable hardware this may not be a limitation for a single simulation. However, any extensive analysis such as a Monte-Carlo simulation would be impractical.

High-fidelity simulations are practical for short simulations spanning hours that are used to collect noise statistics for injecting position noise [8]. This approach has questionable validity during periods where error characteristics may be changing. Our contribution is a physically-motivated approximate pulsar navigation model (APNM) of phase errors that is less computationally expensive than a full fidelity model which counts individual photons, but provides better performance predictions than Gaussian noise models.

This paper will first, briefly, cover the principles which govern and enable pulsar navigation. Then, the approximate and the high fidelity models used will be defined.

Abbreviation: OD, Orbit determination; PN, Pulsar navigation

☆ This paper was presented during the 65th IAC in Toronto

* Corresponding author. Tel.: +16475210614.
E-mail address: ilija.jovanovic@ryerson.ca (I. Jovanovic).

http://dx.doi.org/10.1016/j.actaastro.2015.11.005

Table 1
Uncertainties of OD systems.

System	Uncertainty	Author
Pulsar navigation (best)	100 m	Ashby [7]
SPS GPS (LEO, Worst)	7.8 m	Stenbit [1]
2-Way Doppler, ΔDOR, Ranging (1 AU)	22 m	Kruizinga [3]

Finally, simulation comparisons between the two models and a Gaussian noise model will be presented.

1.1. Motivation

The development of the APNM was motivated by a desire to simulate a PN system for a period of several weeks. The predicted errors of such a simulation would be used to model random position noise for more extensive periods. However, high fidelity simulation of several weeks would still take prohibitively long. Listing the compatibility between duration and models:

- *Hours*: High fidelity model.
- *Weeks*: APNM.
- *Years*: Gaussian noise model.

The APNM would offer an acceptable compromise between highly realistic simulation and computational costs. In addition, missions lasting several years would need their position error models updated periodically to reflect changes in accuracy and precision. The APNM could be used to update the error models of prolonged simulations more frequently.

2. Background

Comparing the high fidelity and the APNM requires understanding of the qualitative differences between the two. It is thus important for us to understand the effect of abstracting processes in the high fidelity model when creating an approximate one.

2.1. Pulsar stars

Pulsars are spinning neutron stars which emit high intensity beams of radiation from their magnetic poles. When their axis of rotation is not aligned with their poles, the spinning may cause the radiation beams to periodically face our solar system. We can detect this as periodic peaks of the star's brightness [5,2].

Rotation-powered and old accretion-powered pulsars have exceedingly stable rotation periods, making PN with them possible [2,9]. A special subset of these are millisecond pulsars which have periods of less than 20 ms along with high rotational stability.

The timing stability of these pulsars is comparable to atomic clocks and permits the signal to be used in orbit determination [7]. The time interval between pulses is stable enough that a change in the signal phase is more likely due to the observer having moved relative to the pulsar than timing noise. The ROSAT and ASCA missions have discovered 27 pulsars, ten of which have desirable stability and spectrums for navigation [9,10].

2.2. Detectors

Pulsars emit broadband radiation with the X-ray spectrum being the more favourable for the smaller detectors [9]. This paper will focus on X-ray based navigation although radio based navigation is possible [9]. The X-ray detector types with desirable size, functionality, and spectral range all have limited time resolution [11]. This resolution imposes a minimum time between subsequent photon counts. If two or more photons arrive within this minimum time period, the detector will still measure a single photon [2,9,11].

Lastly, it is important that the pulsars have appropriate signal to noise ratios (SNR). This depends on the baffle and field of view of the detector as well as the region of space the star is located [2,9]. Even with appropriate detectors and quiet regions of space long (10 min) integration periods are necessary [7,9].

3. Models

This section develops the two models that will be compared. Our high fidelity model simulates individual photon arrivals and detector time resolution. This is the typical approach to modelling short-term PN. Our approximate model, APNM, attempts to mimic the above model without simulating random photon arrivals at the detector's resolution limit.

3.1. High fidelity model

The high fidelity model attempts to account for as many physical phenomena as necessary in order to serve as a benchmark. This model is based on the model presented by Sala et al. [9].

3.1.1. Pulsar simulation

The pulsar's profile is the probabilistic distribution of detecting a photon from the pulsar at any time during a pulse period. It will be represented as a Poisson point process $P(t)$, in units of photon counts per second, where t is time. Since a pulsar's signal periodically repeats, the expected value of P repeats every pulse period, T_p. This can be represented in equation from as

$$\langle P(t+T_p)\rangle = \langle P(t)\rangle \tag{1}$$

The angled brackets, $\langle f\rangle$, represent the expected value of f. Since the simulation is advanced in time steps, $\langle P(t)\rangle$ is approximated as having a linear flux and then averaged over each time step.

Because photon arrivals need to be integrated over prolonged periods of time, the time bins, each defined as an element of vector b with units of photon counts, periodically repeat. Letting b_j represent the count of the time

bin β_j:

$$\beta_j(t+T_p)=\beta_j(t) \tag{2}$$

At this point it becomes necessary to define the different times which are tracked by the model. The solar system's barycentric time, t_{SSB}, and the spacecraft's time, t_c, are related as

$$\Delta t_{SSB}=\gamma\Delta t_c \tag{3}$$

where γ is the Lorentz factor:

$$\gamma=\frac{1}{\sqrt{1-\left(\frac{v}{c}\right)^2}} \tag{4}$$

Detector resolution limits the time step of the simulation and, since the detector is in the spacecraft's frame, the simulation time is chosen to advance in the spacecraft's frame. A step size, δt_c, of 10^{-6} s is selected [11]. During this period of time, the detector can only count one photon. If more than one photon arrives, only the first will be counted. This causes a loss of photon counts during periods of high flux relative to periods of low flux. Combining this with Eqs. (2) and (3), the total counts in a bin at the end of an integration period is

$$b_j=\sum_{\{i|j\}}\min(P(i\delta t_{SSB,E})\delta t_{SSB,E},1) \tag{5}$$

given,

$$i=\{i|(j-1)\Delta t_b<i\delta t_c\le j\Delta t_b, i\in\mathbb{N}\}$$
$$i=\{i|0\le i\delta t_c<T_I, i\in\mathbb{N}\}$$
$$j=1,2,3,\ldots,j_{\max}$$

where T_I is the integration period and Δt_b is the duration of a time bin, both of which are in the spacecraft's time frame, and j is the time bin index. The Lorentz factor estimated by the spacecraft, γ_e, is updated with position and velocity information obtained at the end of each integration period. The integer set i represents all times $i\delta t_{SSB,E}$ which were grouped into bin b_j. Lastly, $\delta t_{SSB,E}$ is the effective barycentric time step which accounts for the spacecraft's relative velocity to the pulsar:

$$t_{SSB,E}=t_{SSB}\left(\frac{\mathbf{v}\cdot\mathbf{u}+c}{c}\right) \tag{6}$$

Here, $\mathbf{v}$ is the spacecraft's velocity vector, $\mathbf{u}$ is a unit vector pointing towards the pulsar, and c is the speed of light.

Evaluating the bins in this manner allows us to determine the total number of counts for each bin at the end of the integration period, represented above as b. This is the information needed to solve for the spacecraft's motion.

3.1.2. Spacecraft simulation

The spacecraft model replicates how the information provided by the above pulsar model is processed. Since Δt_b is in the spacecraft frame, it must be corrected for the spacecraft's motion.

$$\Delta t_b=\frac{T_p}{j_{\max}}\gamma_e^{-1}\left(\frac{c}{\mathbf{v}_e\cdot\mathbf{u}+c}\right) \tag{7}$$

where $\mathbf{v}_e$ is the spacecraft's estimated barycentric velocity, updated once every integration period.

At the end of the integration period the bin counts, b and the known profile, $\langle P(t)\rangle$ are cross correlated. The phase at which the correlation is maximum, Φ_X, is differenced with the phase of the expected profile's peak, Φ_E to obtain the half phase shift for the integration period:

$$\frac{1}{2}\Phi_P=\Phi_X-\Phi_E \tag{8}$$

Although these relations do include velocity, acceleration over the course of the integration period will "smear" the profile of b. In other words, photons will be recorded earlier or later then they otherwise would. Any un-modelled dynamics will appear as a change in the smearing. Ultimately, smearing moves the phase of the recorded profile's peak away from Φ_E.

For the case of un-modelled acceleration, the spacecraft assumes that this smearing occurs monotonically with time and that it can be approximated as linear. So long as this assumption is valid, the epoch of $\Phi_{P/2}$ is the midpoint of the integration period. The phase shift at the end of the period is then

$$\Phi_P=2\Phi_{P/2} \tag{9}$$

where Φ_P is the unit-less normalized phase change. The spatial phase change over the integration period becomes

$$\Delta\Phi_L=\Phi_P T_p c+(\mathbf{v}_e\cdot\mathbf{u})T_I\gamma_e \tag{10}$$

Equation (10) also establishes the sign convention for Φ_P, that is, delayed pulse arrivals result in a negative Φ_P.

Having information from at least three unique pulsars, the change in position over the course of the integration period, $\Delta\mathbf{s}_n$, can be obtained by solving.

Observations of different pulsars yield systems of equations that must hold true simultaneously:

$$\begin{bmatrix}\mathbf{u}_1\\ \mathbf{u}_2\\ \mathbf{u}_3\end{bmatrix}(\mathbf{s}_n-\mathbf{s}_{n-1})=\begin{bmatrix}\Delta\Phi_L^1\\ \Delta\Phi_L^2\\ \Delta\Phi_L^3\end{bmatrix} \tag{11}$$

or more compactly as,

$$\underline{\mathbf{u}}\Delta\mathbf{s}_n=\Delta\underline{\Phi}_L \tag{12}$$

where $\Delta\mathbf{s}_n$ is the change in position during the integration period.

If we can observe at least three pulsars, we can solve for the vector displacement:

$$\Delta\mathbf{s}_n=\underline{\mathbf{u}}^{-1}\Delta\underline{\Phi}_L \tag{13}$$

from here, the spacecraft position is obtained by adding the vector $\Delta\mathbf{s}_n$ to the spacecraft position estimate at the start of integration period {n}.

3.2. Approximate pulsar navigation model

With the APNM, we wish to substitute the output of the high fidelity model: a pulse profile in the form of bin counts, b. The APNM abstracts the photon arrivals, replacing the pulse profile with a single "photon" arriving every pulse period. This creates the desired arrival profile over

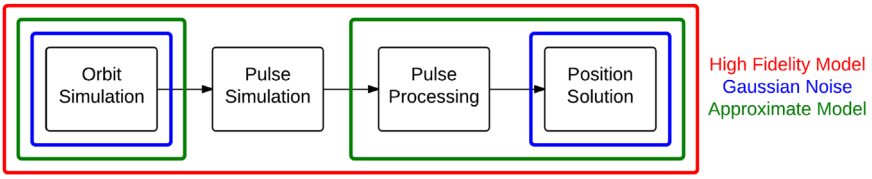

Fig. 1. A top level flow chart showing which processes are considered by the three PN models. The outer enclosure (red) is for the high fidelity model, the middle enclosure (green) is for the APNM, and the inner enclosure (blue) is for Gaussian noise model. (For interpretation of the references to colour in this figure caption, the reader is referred to the web version of this paper.)

the course of an integration period. It also enables larger time steps by removing the constraint imposed by the detector's time resolution. Fig. 1 illustrates the process considered by the APNM relative to the other models discussed.

The rest of this section will develop the framework for the APNM.

3.2.1. Pulsar simulation

Knowing that the approximate model represents the pulse as a single photon, these single photons can be binned to create a profile whose shape is dependent of the motion of the spacecraft. This profile is the desired output of the APNM.

The phase of the pulsar is treated as a continuously increasing number, ϕ_T. The rate of change of ϕ_T is dependent on both time and motion, hence increasing for speeds lower than that of light. Knowing that ϕ_T is in normalized phase units, every time the rounded down integer value of ϕ_T changes, a new pulse has arrived:

$$\phi_T = \frac{\mathbf{u}\cdot\Delta\mathbf{s}}{T_p c} + \frac{t_{SSB}}{T_p} \tag{14}$$

Assuming the binning of the pulse arrivals starts when t_{SSB} is zero, pulses are expected to arrive at bin zero, leaving the potential for negative arrival bins. To avoid the need for special logic to account for arrival bin wrapping, the expected bin is set to the middle bin $0.5j_{\max}$. Similarly, the expected arrival is changed such that it occurs in the middle of a bin instead of the edge of one, avoiding a bi-stable start. Thus, Eq. (14) becomes

$$\phi_T = \frac{\mathbf{u}\cdot\Delta\mathbf{s}}{T_p c} + \frac{t_{SSB}+0.5\Delta t_b}{T_p} - 0.5 \tag{15}$$

Assuming $\Delta\mathbf{s}$ of the orbit can be calculated for any time period without prior knowledge, Eq. (15) becomes deterministic. This comes from the time at which photon i being equal to the time t_{SSB} when $\phi_T = i$ and time bin which correspond to the arrival also being determined by t_{SSB}.

3.2.2. Spacecraft simulation

The second part of the approximation deals with how the information is processed, referred to as the spacecraft model. It deals with integrating pulse arrivals into the appropriate time bin b_j. After each pulse arrives and is recorded to the appropriate bin, for the next pulse, the current time bin is set to the expected one, defined as $0.5j_{\max}$ or simply β_0. This makes every arrival bin b_j relative to the previous. Doppler effects being ignored, the spacecraft does not need knowledge of its own velocity to record a pulse profile. Implicit in this analysis is the assumption that the motion during an integration period must be less than half of a pulse width. Because this would correspond to an average velocity of about $0.5c$, it will not be a practical limitation in foreseeable systems.

The phase shift relative to the integration period's starting epoch, measured in bins, of the ith pulse can be rewritten as

$$\beta_i = (\beta_{1|0} - \beta_0) + \cdots + (\beta_{i|i-1} - \beta_0) \tag{16}$$

where $\beta_{i|i-1}$ is the arrival bin, j, of the ith pulse relative to the previous pulse. Equation (16) can be shortened to

$$\beta_i = \sum_{k=1}^{i} \beta_{k|k-1} - i\beta_0 \tag{17}$$

Equation (17) is not deterministic although that is not to say it cannot be. Computation time of the approximate model was not a limiting factor so efficient implementation was not a major concern. An important distinction to note is that β_i is a bin number while b_j is the photon counts in bin j. The reason the arrival pulses are not simply binned as they are in the high fidelity model is that the value of β_i can exceed $j_{\max}$. This way, arrival bins do not wrap with pulse number; this is illustrated in Fig. 2.

To better explain the wrapping, consider a pulsar's signal, simulated using Eq. (15) and integrated by a spacecraft moving at constant velocity for some period of time. The integration time is long enough that there is a substantial change in phase. Although the spacecraft is not accelerating, the approximate model does not account for velocity, allowing Doppler effects to smear the phase; otherwise all the photons would arrive in the expected arrival bin. The photon arrivals are processed into eight bins according to Eq. (17). The result of this is shown in Fig. 2.

By recording the arrival bins to β_i, the data are already unwrapped (Fig. 2), otherwise, the counts of bins nine and ten would be in bins one and two. The distribution is symmetric since, for constant velocity, the Doppler smearing happens at a constant rate. Fig. 2 shows an arbitrarily shaped symmetric distribution fitted to the data. The first and last bins to record pulses have fewer counts than the other bins due to there being no constraint on the start and stop time of the integration period in relation to the time bins. Having established this, the change in spatial phase is

$$\Delta\Phi_L = -2\overline{\beta}_i \frac{T_p}{j_{\max}} c \tag{18}$$

where $\overline{\beta}_i$ is the mean value of β_i. The coefficient of two in Eq. (18) comes from the epoch of $\overline{\beta}_i$ being the half-way point of the integration period.

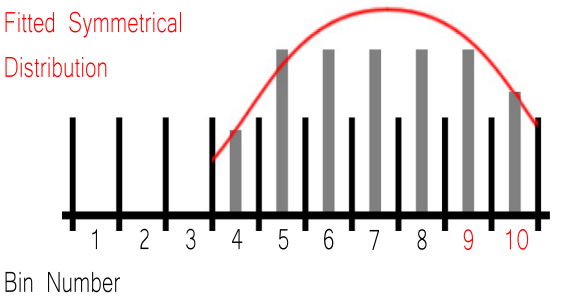

Fig. 2. Histogram of pulse arrival counts of the bins, β_i, where the pulse period is divided into eight time bins and the spacecraft velocity is constant. The last two time bins (red) exist to prevent wrapping. (For interpretation of the references to colour in this figure caption, the reader is referred to the web version of this paper.)

Lastly, the time bin size for the approximate model is

$$\Delta t_b = \frac{T_p}{j_{\max}\gamma_e} \tag{19}$$

3.3. Model comparison

In this section, the above models will be conceptually compared to more clearly identify where they are similar and where they vary. Their differences are particularly important since they will be the source of discrepancy between the two models.

3.3.1. Acceleration

Neither of the models account for any acceleration, however, the effects of acceleration appear differently in the two models.

In the approximate model, acceleration causes the pulse arrival rate to gradually evolve. Considering Fig. 2, if acceleration were added, bins five to nine would not all contain the same number of pulses. Instead, for constant acceleration, a trapezoidal shape would be prominent, as shown in Fig. 3. In the case of Fig. 3, the spacecraft is accelerating towards the pulsar. Thus, the later bins, on the right, have higher counts. This is the result of the spacecraft travelling into the pulses at a greater rate.

In the APNM, if the acceleration is small enough relative to the velocity and integration period, the effects of acceleration will be reduced. One can predict the effect this will have on $\overline{\beta}_i$ by comparing the expected number of counts per bin, $\mathcal{C}(t)$, at the start and end of the integration period. A general equation for number of counts is

$$\mathcal{C}(t) = \frac{1}{T_p} + \frac{\mathbf{v}(t)\cdot\mathbf{u}}{cT_p} \tag{20}$$

As an example, given constant acceleration $\mathbf{v}(t) = at$ such as the case of Fig. 3, Eq. (20) becomes

$$\mathcal{C}(t) = \frac{1}{T_p} + \frac{at}{cT_p} \tag{21}$$

which is a linearly changing count rate.

In the case of the high fidelity model, since the expected pulse is Doppler corrected, any motion in the phase will be the direct result of acceleration with no attenuation.

3.3.2. Noise

The high fidelity model has noise introduced by a Poisson point processes used to generate photon counts. The APNM, however, has no random process. Instead of timing noise, the truncation noise of the first and last bins acts as substitute.

3.3.3. Neglected effects

Neither of the models account for gravitational time dilation since the error it introduces will be negligible for a heliocentric orbit over the course of 30 min. Moreover, the difference between the effect it will have on the high fidelity model versus the APNM is even less significant. For a heliocentric orbit lasting 30 min and passing the orbit of Jupiter with an orbital radius of 10^9 km and an orbital speed of 16 km/s, velocity will have changed by roughly $\mu r^{-2}\Delta t = 3.9$ m/s or $0.25\times10^{-3}\%$ while gravitational potential changes by $\mu(r^{-1}+(r-v\Delta t)^{-1}) = 0.063$ km^2 s^{-2} or $0.037\times10^{-3}\%$. Thus, gravitational time dilation will have a ten times smaller effect than time dilation caused by relative velocity. In a real world missions spanning many months, it is imperative that gravitational time dilation is accounted for [2,8].

Proper motion of the pulsars is another important factor in real world missions lasting months or years but has negligible influence over 30 min, the duration of the simulation. Assuming a proper motion of 25 mas yr^{-1} [12], a real world mission lasting 20 years would have accumulated roughly ten meters of error per pulsar. While somewhat significant, error accumulated in 30 min of simulation from proper motion would be less than 30 nm per pulsar. As a result, neither model will account for proper motion.

4. Simulations

The results of comparative tests of the models, along with parameters used to generate the tests are presented in this section. The first part of this section will look at the formulation of the simulations. This will be followed by a summary of the results.

4.1. Formulation

Navigation errors are functions of the accuracy of the phase measurements and the geometric distribution of pulsars on the celestial sphere. To minimize the latter effect, we formulate an artificial set of three pulsars located in orthogonal directions along the barycentric frame axes. These pulsars all have the same typical single-peak profiles shown in Fig. 4. The pulse width is selected to resemble the X-ray spectrum pulse profiles of real pulsars [2,10,13]. Added to the profile is a DC-level representing background noise. The amount of background noise added depends on the signal to noise ratio (SNR) of the simulation.

The pulse periods are randomized, to represent the asynchronous nature of real data. All the periods are within 20% of the average pulse period. Although the ideal pulsars for this application are millisecond pulsars [5,2,4,9], simulation of higher frequency information is computationally demanding. For this reason, millisecond pulsars are only used in one of the comparative tests. For the remainder of the parameters, unless

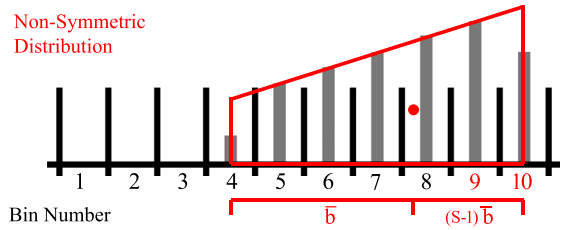

Fig. 3. Non-symmetric distribution approximated by a trapezoid. The red dot represents the centroid of the shape, $\overline{\beta}_i$. (For interpretation of the references to colour in this figure caption, the reader is referred to the web version of this paper.)

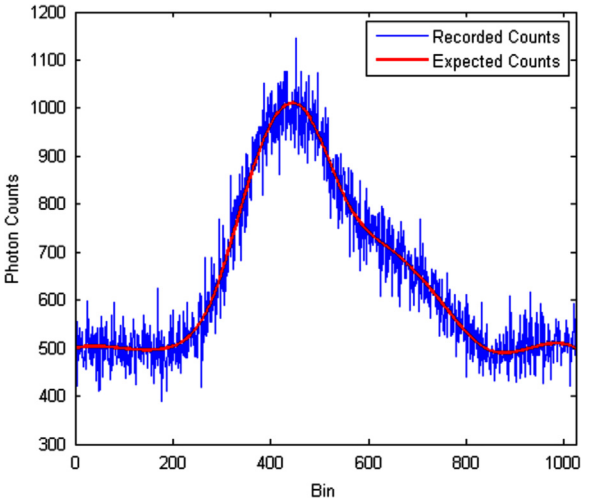

Fig. 4. Expected and recorded bin counts for an integration period of six minutes. The profile has 1024 bins per pulse and a 1000 count per bin peak. This is a synthetic pulse profile characteristic of X-ray pulsars [2,10,13].

Table 2
Default simulation parameters.

Parameter	Value
Bins per pulse	1024
SNR	1
Integration period	6 min
Average pulse period	0.3 s
Peak counts per second	1000 counts/s

it is otherwise specified, the simulation configuration is as outlined in Table 2.

Two missions will be looked at in the following sections. Mission-1 will be a 36 min Earth to Mars two-body Hohmann transfer. The simulation is initialized when the spacecraft is at Earth's perihelion and beyond Earth's sphere of influence. Mission-2 will be an Earth to Moon Hohmann transfer initializing when the spacecraft leaves its parking orbit in LEO. Table 3 can be used for quick reference.

4.2. Testing and results

This section will present the effect pulse period, brightness, integration time, and binning have on the position errors of both models. The purpose of this testing is to establish the conditions in which the approximate model is a valid substitute. Knowing the true position of the simulated satellite, the position errors in this section are always relative to the true position. Every data point presented in this section is the mean final position error from six independent simulations.

Table 3
Quick reference for missions one and two.

Mission-1	Earth to Mars Hohmann transfer
Mission-2	LEO to Moon Hohmann transfer

4.2.1. Tests

The purpose and description of each of the five tests:

1. *High fidelity model validation*:
   The purpose of this test is to validate the implementation of the high fidelity model. This is done by removing all timing noise and replacing it with an exact and continuous stream of photons. The photon flux is made identical to the pulse profile. The only source of error left was the loss of photons from the detector's time resolution and errors from the unmodelled acceleration. If the implementation was done well, the position should be on the order of 100 m [7].
2. *Integration time*:
   The purpose of this test was to look for correlated trends in position errors between the APNM and the high fidelity model when integration time is varied. Since the APNM is physically motivated, it is desirable to confirm its behaviour when parameters such as integration time are changed. For this test, position errors of both models were recorded using a set of integration times.
3. *Bins per pulse*:
   Similarly to test two, this test's purpose was to look for correlated trends in position error when the bin division per pulse were varied. The motivation for this also being to ensure the APNM is characteristic of the physical system.
4. *Millisecond pulsars*:
   This test was done to see if increasing the number of integrated pulses by raising the pulse frequency would bring the average error of the two models closer together. This has the same effect as increasing integration time but without the increased error propagation caused by a longer gap between position updates. Simulating higher frequency data is more computationally demanding so only one data point was collected. This test used pulsars with mean frequencies of 30 ms. Although not strictly millisecond pulsars, their frequency is close to that of the 33 ms Crab pulsar, a very bright and stable X-ray pulsar [13].
5. *Ultra-bright pulsars*:
   This test is similar in concept to test four except the pulsars are made brighter instead of faster. More photons are captured and timing noise is attenuated, giving the effect of a longer integration period. Unlike test four, increasing the count had no effect on simulation speed and more test could be conducted. For this test, the peak brightness of the pulsar was raised to 100,000 counts/s with a SNR of 10. This is not designed to mimic real pulsars, instead, it is a proof of concept: that attenuating timing noise without reducing

the standard deviation or altering pulse frequency brings the performance of the two models closer together.

4.2.2. Results

1. *High fidelity model validation*:
   Under these conditions, the mean position error predicted by the model was 86 m with a standard deviation of 67 m. This is orders of magnitude smaller than the results with timing noise, suggesting a larger component of the position error is unbiased timing noise.
2. *Integration time*:
   Fig. 5 shows an increase in position errors of the high fidelity model for the longer integration time. This is expected since longer integration times attenuate the effects of measurement noise but also reduce the frequency of position updates. Lowering the integration time increases the frequency of position updates, reducing perturbations created by un-modelled dynamics.
3. *Bins per pulse*:
   From Fig. 6, for fewer bin divisions, the APNM's error increases more than the high fidelity model's error, almost overtaking it at 128 bins per pulse. Both models are expected to exhibit increases in uncertainty as the bin size increases due to the resolution of the information being decreased. The APNM also has uncertainty from the truncation of the perimeter time bins. As the number of bins decreases, truncated values form a larger portion of the total information. However, where the two models begin to agree, at 128 bins per pulse, precision navigation would be very difficult.
4. *Millisecond pulsars*:
   The results shown in Table 4 suggest that the two models are closer in performance when using millisecond pulsars. Timing being the largest change when using millisecond pulsars, this result further supports that the difference between the two models is unbiased noise.
5. *Ultra-bright pulsars*:
   Table 5 shows the models having the same reduced performance gap seen in Table 4. Again, this result supports that the difference between the models is timing noise.

4.3. Increasing the APNM's uncertainty

As discussed previously, one of the differences between the two models is that the APNM substitutes Poisson random noise with truncation errors of the first and last bins. The millisecond pulsar and ultra-bright pulsar test demonstrated that by effectively increasing integration times, the two models begin to approach one another. Underlying this is that longer integration times reduce timing noise, and hence phase errors. The validation test demonstrate the performance improvement possible in the high fidelity model with the removal of timing noise.

Since reducing timing noise in the high fidelity model brings it closer to APNM, increasing the APNM's timing noise would provide the desired result of bringing it closer in performance to the high fidelity model. In other words, the truncation error in the APNM has proven to be much smaller than the timing noise of the high fidelity model.

The mean timing truncation error of the approximate model zero but the probability of it being non-zero can be modelled as

$$P(b_{\min} - b_{\max} = k) = \sum_{l=0}^{i_{\max}-k} Ps(k+l)Ps(l) \tag{22}$$

where $b_{\min}$ and $b_{\max}$ denote the randomly distributed arrival counts of the two perimeter bins, and $i_{\max}$ is the number of bins separating $b_{\min}$ and $b_{\max}$. Finally, $Ps(x)$ is the Poisson probability of a x counts:

$$Ps(x) = \frac{\mathcal{C}(t)^x e^{-\mathcal{C}(t)}}{x!} \tag{23}$$

The variance of Eq. (22) can be approximated as

$$Var(b_{\min} - b_{\max}) = \tfrac{1}{2}\overline{\mathcal{C}} - 2(b_{\min} * b_{\max}) \tag{24}$$

where $\overline{\mathcal{C}}$ is the average expected counts per bin.

From here, the timing noise of the high fidelity model was isolated using a constant velocity simulation. This was differenced from the $1-\sigma$ estimate of Eqs. (22) and (24), giving the timing noise discrepancy between the two models.

Table 6 shows the performances of the two models when this discrepancy is added as zero-mean Gaussian noise to the approximate model's phase estimates.

The necessary noise injection is, ideally, not dependent on the mission state. So, as long as the simulated hardware is not changed and the same pulsars are being used, high fidelity simulation is only necessary for an initial calibration.

4.4. Gaussian noise model comparative test case

The above results suggest that a substantial portion of position error for the high fidelity model comes from timing noise and that the approximate model would need to primarily consist of supplemented noise in order to match the position errors of the high fidelity model. That being the case, one would question the advantage of the APNM over a simple Gaussian noise model. Despite most of the position error being randomly generated, the APNM would still have biased errors that are characteristic of the system which no filtering could remove. The Gaussian noise model could be filtered to provide a very close to true position estimate.

To demonstrate this behaviour, Mission-2 will be used. The scenario will simulate the first ten hours of the transfer and compare the performance of the APNM to the Gaussian model. Beforehand, each model will be calibrated against a high fidelity model simulation of the first 36 min in LEO. Since the Gaussian model tracks orbital acceleration, an acceleration correction such as the one in Fig. 3 was added to the APNM. This scenario was selected since the acceleration of the orbit quickly decreases, effecting the validity of any calibration done using a higher fidelity model.

The goal of the test is to demonstrate that the Gaussian model and APNM will have different trends under rapidly changing orbital acceleration. Due to computational limitations of running the high fidelity model multiple times, a coarse calibrations for the two models was done. We feel this an

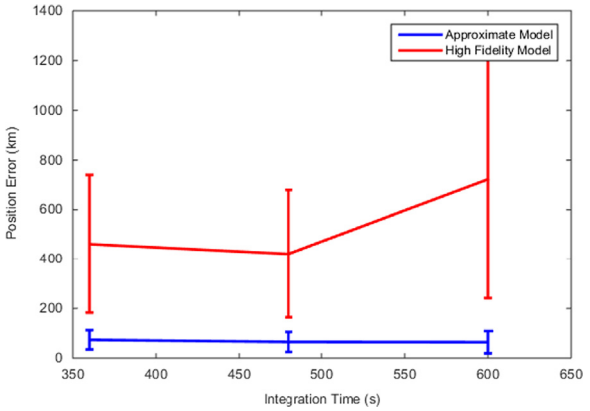

Fig. 5. Position errors for both models as functions of integration time using Mission-1.

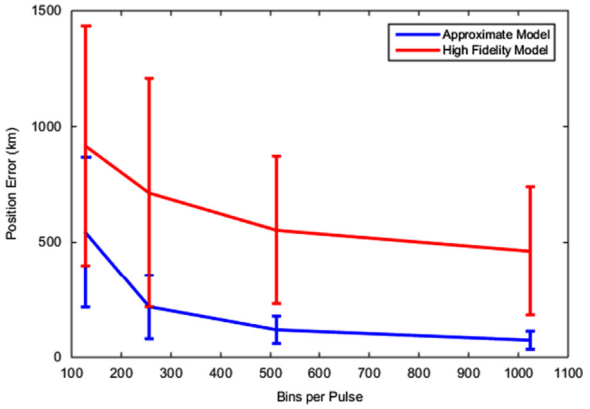

Fig. 6. Position errors for both models as functions of the number of bin divisions per pulse using Mission-1.

Table 4
Position errors using millisecond pulsars using Mission-1.

Model	Mean uncertainty (km)	Standard deviation (km)
APNM	74	42
High fidelity model	105	61

Table 5
Position errors using ultra-bright pulsars using Mission-1.

Model	Mean uncertainty (km)	Standard deviation (km)
APNM	74	42
High fidelity model	115	58

Table 6
Position errors with noise added to approximate model using Mission-1.

Model	Mean uncertainty (km)	Standard deviation (km)
Approximate model	621	370
High fidelity model	576	280

Table 7
Position errors for calibrated approximate and Gaussian noise models for the first 36 min using Mission-2.

Model	Mean uncertainty (km)
High fidelity model benchmark	400
Calibrated APNM	520
Calibrated Gaussian noise model	644

Table 8
Position errors for calibrated approximate and Gaussian noise models for the first ten hours using Mission-2.

Model	Mean uncertainty (km)
Calibrated approximate model	363
Calibrated Gaussian noise model	775

Table 9
Optimal position measurement uncertainty for Kalman filtering.

Model	Optimal position measurement uncertainty (km)		
	Simulation 1	Simulation 2	Simulation 3
APNM	12,247	3824	13,132
Gaussian noise model	4989	8994	1162

acceptable compromise since the goal is not to demonstrate fine calibration. Table 7 shows the results of the calibration.

Table 8 shows their mean position errors after three simulations of the first ten hours for each model. The results agree with the expected result: that the position error of the APNM would decrease more than that of the Gaussian noise model as the orbital acceleration decreased. Again, this is due to acceleration being an un-modelled dynamic, thus, as its effect decreased so did the errors. Regardless which dynamics are un-modelled, this test demonstrated that the APNM has a ability to react to changes in those dynamics; the Gaussian noise model inherently does not.

With knowledge of the true position at any instant, a discrete-time extended Kalman filter had its measurement noise parameters optimized using position estimates provided by each model. The dynamics and measurement functions, f and h respectively, of the filter are

$$\dot{\mathbf{x}}_k = f(\mathbf{x}_{k-1}) = \begin{bmatrix} 0 \\ 0 \\ \dot{M}_{k-1} \end{bmatrix}, \quad h(\mathbf{x}_k) = \Delta\mathbf{s}_k \tag{25}$$

where $\dot{M}_{k-1}$ is the rate of change in true anomaly. The displacement vector $\Delta\mathbf{s}_k$ is taken in the pericentric frame, thus the z-component is ignored. Consequently, the state vector, $\mathbf{x}_k$ is

$$\mathbf{x}_k = \begin{bmatrix} a \\ e \\ M_k \end{bmatrix} \tag{26}$$

where e is the orbital eccentricity and a is the semi-major axis.

This was done for the three simulations used in Table 8 and the results are given in Table 9.

Two of the simulations agree with the prediction at the start of this section: the higher position errors of the Gaussian model (see Table 8) can be filtered (see Table 9) while the APNM has biased errors which could not. The significance of the results of simulation one and two are that, in comparison to the Gaussian model, the errors of the calibrated APNM contain a measurable bias. So, despite the position errors of the calibrated APNM being mostly noise, the model can still characterise the effects of un-modelled dynamics.

5. Conclusions

It was demonstrated that by supplementing the approximate model with noise, its performance can approach that of the high fidelity model. Based on the validation test, PN is inherently dominated by noise in the short term, implying that some level of added noise to the approximate model is not ill-suited. Simulating only noise would not capture the nuances of the system's interaction with un-modelled dynamics or non-orthogonal navigation pulsars. The influence and presence of these dynamics in the approximate model was demonstrated using the comparative test case. High pulse frequency PN is more accurately modelled by our approximation, requiring far less noise to be added. Lastly, more accurate estimators which allow for longer integration without increased perturbations would see a reduced performance gap between the high fidelity and approximate models. The approximate model can be used to simulate PN with accuracy and speed suitable for simulations lasting several weeks.

Appendix A. Supplementary data

Supplementary data associated with this article can be found in the online version at http://dx.doi.org/10.1016/j.actaastro.2015.11.005.

References

[1] Assistant secretary of defense for command, control, communications, and intelligence, Global positioning system standard positioning service performance standard, 4th ed, Technical Report, 2001.

[2] S. Sheikh, D.J. Pines, Spacecraft navigation using x-ray pulsars, J. Guid. Control Dyn. 29 (1) (2006) 49–63.

[3] G.L. Kruizinga, E.D. Gustafson, Mars science laboratory interplanetary navigation analysis, In: 32nd International Symposium on Space Flight Dynamics, Pasadena, CA, 2012.

[4] N. Ashby, A.R. Golsham, et al., Minimum uncertainties in position and velocity determination using x-ray photons from millisecond pulsars, In: Proceedings of the 2008 National Technical Meeting of the Institute of Navigation, San Diego, CA, 2008.

[5] P. Graven, J. Collins, S. Sheikh, J. Hanson, P. Ray, K. Wood, Xnav for deep space navigation, In: 31st Annual AAS Guidance and Control Conference, AAS, Breckenridge, CO, 2008.

[6] T.J. Chester, S.A. Butman, Navigation using x-ray pulsars, Telecommun. Data Acquis. Prog. Rep. 42–63 (1981) 22–25.

[7] N. Ashby, D.A. Howe, Relativity and timing in x-ray pulsar navigation, in: International Frequency Control Symposium and Exposition, Miami, FL, 2006, pp. 767–770.

[8] X.P. Deng, G. Hobbs, et al., Interplanetary spacecraft navigation using pulsars, Adv. Sp. Res. 52 (9) (2013) 1602–1621.

[9] J. Sala, A. Urruela, et al., Pulsar navigation, In: 2nd Workshop on Innovative Concepts, ESA, Noordwijk, The Netherlands, 2008.

[10] W. Becker, J. Trümper, The x-ray emission properties of millisecond pulsars, Astron. Astrophys. 341 (2008) 803–817.

[11] A.C. Thompson, X-ray data booklet: Section 4.5 x-ray detectors, Technical Report, Center for X-Ray Optics and Advanced Light Sources, 2009.

[12] D.J. Nice, J.H. Taylor, Psrs j2019+2425 and j2322+2057 and the proper motions of millisecond pulsars, Astrophys. J. 441 (1995) 429–435.

[13] C. Jain, B. Paul, Pulse profile stability of the crab pulsar, Res. Astron. Astrophys. 11 (10), 2011, 1134-1142.

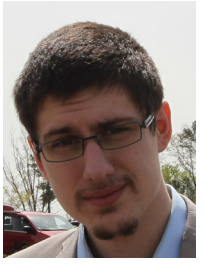

Ilija Jovanovic holds a BEng (2013) and is currently a master's student at Ryerson University, both in the field of aerospace engineering. Ilija's research focuses on the calibration of star trackers, computer modelling of pulsar navigation, and nighttime planetary navigation.

John Enright holds a BASc (1997) from the University of Toronto (Engineering Science: Aerospace) and a MS (1999) and a PhD (2002) from MIT in Aerospace Systems. He is currently an Associate Professor in Aerospace Engineering at Ryerson University in Toronto. Having joined the faculty at Ryerson University in 2003, he is now the Principal Investigator of the Space Avionics and Instrumentation Laboratory (SAIL). Dr. Enright and his SAIL researchers have demonstrated expertise in instrument calibration, attitude estimation and sensor processing algorithms. While at MIT (1999–2003), he led the software development for the SPHERES flight project, and the GFLOPS real-time spacecraft simulation testbed. His research interests include spacecraft avionics and sensor processing, systems engineering and flight software. Dr. Enright is a member of the AIAA, CASI, and the IEEE.